Supplementary Information for

Deciphering the Electronic and Structural Origin of Chiroptical Activity of Chiral 2D Perovskites

Zixuan Zhang, Jin Wu, Haipeng Lu*

Department of Chemistry, The Hong Kong University of Science and Technology, Clear Water Bay, Kowloon, Hong Kong, China (SAR)

Corresponding Author

Haipeng Lu*: haipenglu@ust.hk

Table S1. Crystal data and structure refinement for (*R*-3ClMBA)$_2$PbBr$_4$ and (*R*-3ClMBA)$_2$PbI$_4$

	(*R*-3ClMBA)$_2$PbBr$_4$	(*R*-3ClMBA)$_2$PbI$_4$
Empirical formula	$C_{16}H_{22}Br_4Cl_2N_2Pb$	$C_{16}H_{22}Cl_2I_4N_2Pb$
Formula weight	840.08	1028.04
Temperature	100.00(10) K	99.99(10) K
Wavelength	0.71073 Å	0.71073 Å
Space group	$P2_1$	$P2_1$
Unit cell dimensions	a = 8.7598(2) Å, α = 90° b = 7.7798(2) Å, β = 97.984(2)° c = 17.5050(4) Å, γ = 90°	a = 9.1762(2) Å, α = 90° b = 8.18250(10) Å, β = 98.856(2)° c = 17.4483(3) Å, γ = 90°
Volume	1181.39(5) Å^3	1294.47(4) Å^3
Z	2	2
Density (calculated)	2.362 g/cm^3	2.638 g/cm^3
Absorption coefficient	14.135 mm^{-1}	11.497 mm^{-1}
F(000)	776	920
Crystal size	0.11 x 0.08 x 0.07 mm^3	0.07 x 0.04 x 0.03 mm^3
θ range for data collection	2.348 to 26.731°	2.363 to 26.729°
Reflections collected	7306	8228
Independent reflections	4643 [R_{int} = 0.0255]	4650 [R_{int} = 0.0250]
Data / restraints / parameters	4643 / 7 / 230	4650 / 31 / 230
Goodness-of-fit	1.033	0.999
Final R indices [I > 2σ(I)]	R_{obs} = 0.0307, wR_{obs} = 0.0673	R_{obs} = 0.0227, wR_{obs} = 0.0465
R indices [all data]	R_{all} = 0.0335, wR_{all} = 0.0691	R_{all} = 0.0244, wR_{all} = 0.0473
Largest diff. peak and hole	1.942 and -1.389 e·Å^{-3}	0.713 and -1.229 e·Å^{-3}

[a] $R = \Sigma||F_o|-|F_c|| / \Sigma|F_o|$, $wR = \{\Sigma[w(|F_o|^2 - |F_c|^2)^2] / \Sigma[w(|F_o|^4)]\}^{1/2}$ and $w=1/[\sigma^2(Fo^2)+(0.0325P)^2]$ where $P=(Fo^2+2Fc^2)/3$. [b] $R = \Sigma||F_o|-|F_c|| / \Sigma|F_o|$, $wR = \{\Sigma[w(|F_o|^2 - |F_c|^2)^2] / \Sigma[w(|F_o|^4)]\}^{1/2}$ and $w=1/[\sigma^2(Fo^2)+(0.0171P)^2]$ where $P=(Fo^2+2Fc^2)/3$.

Table S2. Crystal data and structure refinement for (*R*-3BrMBA)$_2$PbBr$_4$ and (*R*-3BrMBA)$_2$PbI$_4$

	(*R*-3BrMBA)$_2$PbBr$_4$	(*R*-3BrMBA)$_2$PbI$_4$
Empirical formula	$C_{16}H_{22}Br_6N_2Pb$	$C_{16}H_{22}Br_2I_4N_2Pb$
Formula weight	929.00	1116.96
Temperature	173.00(10) K	173.00(10) K
Wavelength	1.54184 Å	1.54184 Å
Space group	$P2_1$	$P2_1$
Unit cell dimensions	a = 8.73840(10) Å, α = 90° b = 7.84410(10) Å, β = 97.8460(10)° c = 17.9204(2) Å, γ = 90°	a = 9.1768(2) Å, α = 90° b = 8.2407(2) Å, β = 98.883(2)° c = 17.8463(5) Å, γ = 90°
Volume	1216.85(3) Å^3	1333.40(6) Å^3
Z	2	2
Density (calculated)	2.535 g/cm^3	2.782 g/cm^3
Absorption coefficient	25.048 mm^{-1}	52.197 mm^{-1}
F(000)	848	992
Crystal size	0.2 x 0.18 x 0.03 mm^3	0.03 x 0.03 x 0.02 mm^3
θ range for data collection	2.489 to 74.513°	4.878 to 74.263°
Reflections collected	9475	7755
Independent reflections	4738 [R_{int} = 0.0418]	4452 [R_{int} = 0.0302]
Data / restraints / parameters	4738 / 100 / 230	4452 / 55 / 230
Goodness-of-fit	1.053	1.004
Final R indices [I > 2σ(I)]	R_{obs} = 0.0476, wR_{obs} = 0.1329	R_{obs} = 0.0251, wR_{obs} = 0.0548
R indices [all data]	R_{all} = 0.0482, wR_{all} = 0.1340	R_{all} = 0.0280, wR_{all} = 0.0559
Largest diff. peak and hole	2.918 and -2.067 e·Å^{-3}	1.043 and -0.830 e·Å^{-3}

[a]$R = \Sigma||F_o|-|F_c|| / \Sigma|F_o|$, $wR = \{\Sigma[w(|F_o|^2 - |F_c|^2)^2] / \Sigma[w(|F_o|^4)]\}^{1/2}$ and $w=1/[\sigma^2(Fo^2)+(0.1102P)^2]$ where $P=(Fo^2+2Fc^2)/3$. [b]$R = \Sigma||F_o|-|F_c|| / \Sigma|F_o|$, $wR = \{\Sigma[w(|F_o|^2 - |F_c|^2)^2] / \Sigma[w(|F_o|^4)]\}^{1/2}$ and $w=1/[\sigma^2(Fo^2)+(0.0207P)^2]$ where $P=(Fo^2+2Fc^2)/3$.

Table S3. Crystal data and structure refinement for (*R*-4BrMBA)$_2$PbBr$_4$

	(*R*-4BrMBA)$_2$PbBr$_4$
Empirical formula	$C_{32}H_{48}Br_{12}N_4O_2Pb_2$
Formula weight	1894.04
Temperature	99.99(10) K
Wavelength	0.71073 Å
Space group	$P2_1$
Unit cell dimensions	a = 7.8357(2) Å, α = 90° b = 35.9831(11) Å, β = 90.903(2)° c = 8.8981(2) Å, γ = 90°
Volume	2508.53(11) Å^3
Z	2
Density (calculated)	2.508 g/cm^3
Absorption coefficient	16.292 mm^{-1}
F(000)	1736
Crystal size	0.17 x 0.15 x 0.03 mm^3
θ range for data collection	2.289 to 25.348°
Reflections collected	14228
Independent reflections	7980 [R_{int} = 0.0402]
Data / restraints / parameters	7980 / 219 / 483
Goodness-of-fit	1.102
Final R indices [I > 2σ(I)]	R_{obs} = 0.0508, wR_{obs} = 0.1222
R indices [all data]	R_{all} = 0.0543, wR_{all} = 0.1248
Largest diff. peak and hole	3.143 and -2.295 e·Å^{-3}

$R = \Sigma||F_o|-|F_c|| / \Sigma|F_o|$, $wR = \{\Sigma[w(|F_o|^2 - |F_c|^2)^2] / \Sigma[w(|F_o|^4)]\}^{1/2}$ and $w=1/[\sigma^2(Fo^2)+(0.0583P)^2+30.7291P]$ where $P=(Fo^2+2Fc^2)/3$

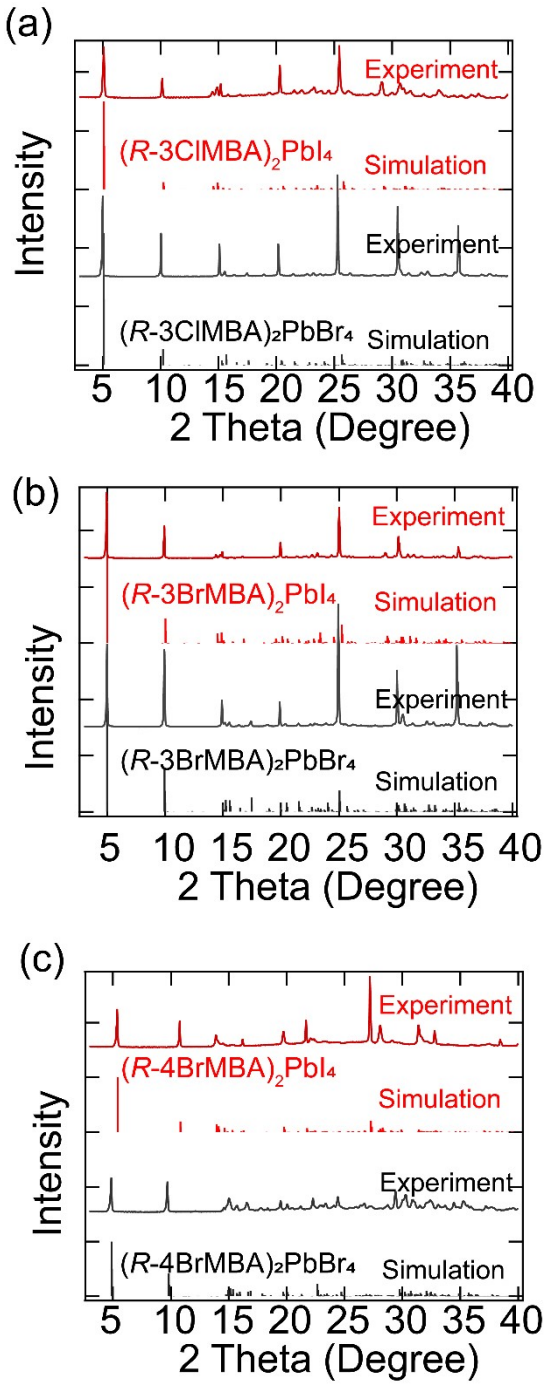

Figure S1. PXRD spectra for (a) **(*R*-3ClMBA)$_2$PbX$_4$**; (b) **(*R*-3BrMBA)$_2$PbX$_4$** perovskites and (c) **(*R*-4BrMBA)$_2$PbX$_4$** (X indicates Br^- and I^- respectively).

Supplementary Information Note I: the mechanism for different CD shapes

If we consider the CD spectra using the same mechanistic picture of MCD, but at zero magnetic field (B=0), we can then apply the theory of MCD for the CD spectra interpretation. While MCD signal originates from the magnetic-field induced Zeeman splitting of the electronic states, CD signal originates from the intrinsic energy splitting or electronic states induced by chirality. The MCD intensity can be simplified by the sum of three Faraday terms, that is, A, B, and C terms:

$$\Delta A = \gamma \mu_B B[A_1\left(-\frac{df(E)}{dE}\right) + \left(B_0 + \frac{C_0}{k_B T}\right) f(E)]$$

Where γ is a constant. μ_B is the Bohr magneton, B is the magnetic field, k_B is the Boltzmann constant, T is the temperature, E is the energy, and f(E) is the line-shape function. A_1, B_0, and C_0 are parameters that describe the A, B, and C terms of MCD, respectively. A, B, and C terms provide information about the Zeeman splitting of degenerate excited states, the field-induced mixing of zero-field states, and the Zeeman splitting based ground state population adjustment, respectively (as shown in the following Figure R1). When the A term is dominant, the CD spectra will be derivative shape, while when the C term is dominant, it will be Gaussian-like shape. We suspect that different chiral cations will modulate the degeneracy of both excited and ground states, that is, the conduction and valence band degeneracy. However, further computational work on the detailed band structure will be needed in order to confirm this.

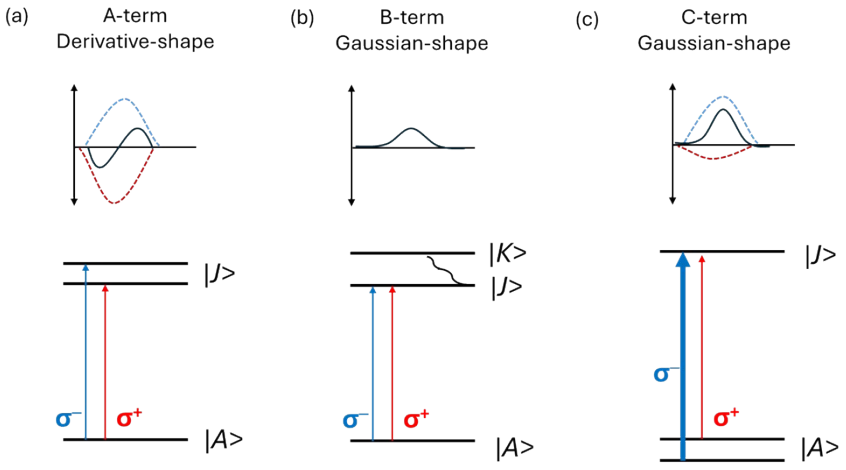

Figure S2. A, B, and C term intensity mechanisms for magnetic circular dichroism (MCD) signal.

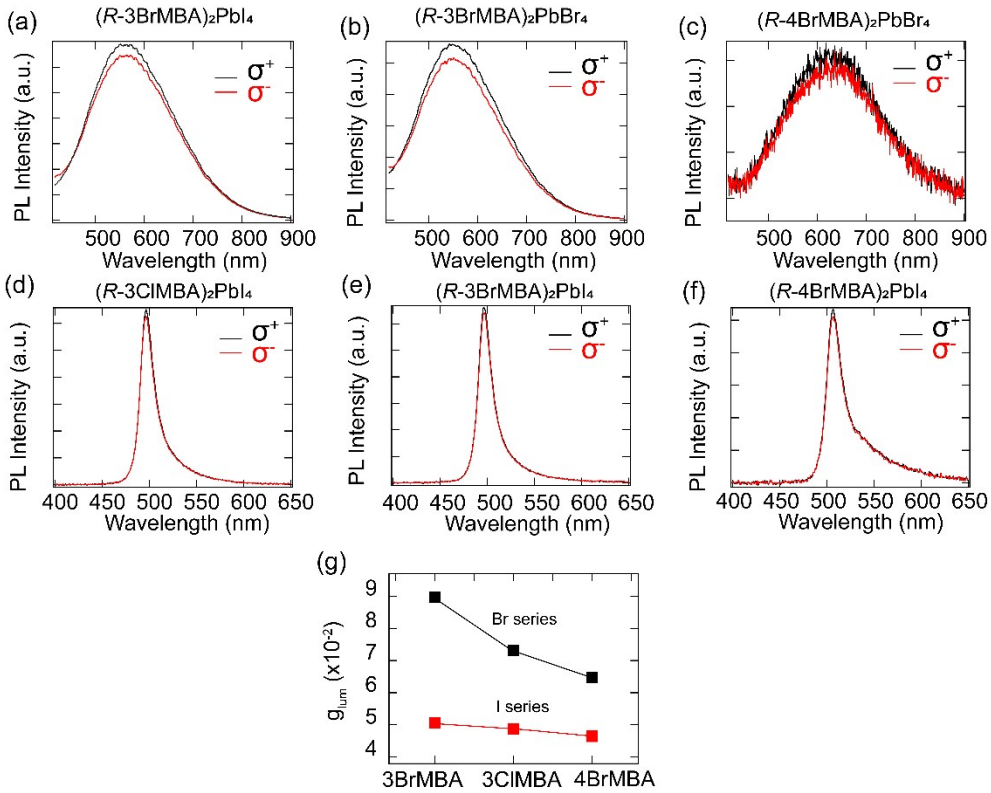

Figure S3. (a)-(f) CPL spectra for chiral 2D perovskites. (g) Dissymmetry factor (g_{lum}) trend summary of Br series and I series perovskites.

Supplementary Information Note II

The CPL dissymmetry factor (g_{lum}) is calculated by **eq 1**, where I_L and I_R represent the intensity of right-handed and left-handed CPL, respectively.

$$g_{lum} = 2 \times \frac{I_L - I_R}{I_L + I_R} \qquad \textbf{Eq. 1}$$

The calculated dissymmetry factor (g_{lum}) value is within 10^{-2} scale (**Figure S2g**), which increase by one order of magnitude compared to the reported 2D lead-based chiral perovskites. Interestingly, the g_{lum} values exhibit the same trend as the g_{CD} values, in which the Br series are larger than I series. The maximum g_{lum} value is obtained as ~0.09 for $(R\text{-3BrMBA})_2PbBr_4$, which is 1.8 times larger than its isostructure $(R\text{-3BrMBA})_2PbI_4$. We attribute different performance of CD and CPL towards different chiral organic cations used, which affects the chiroptical performance via substituents effect.

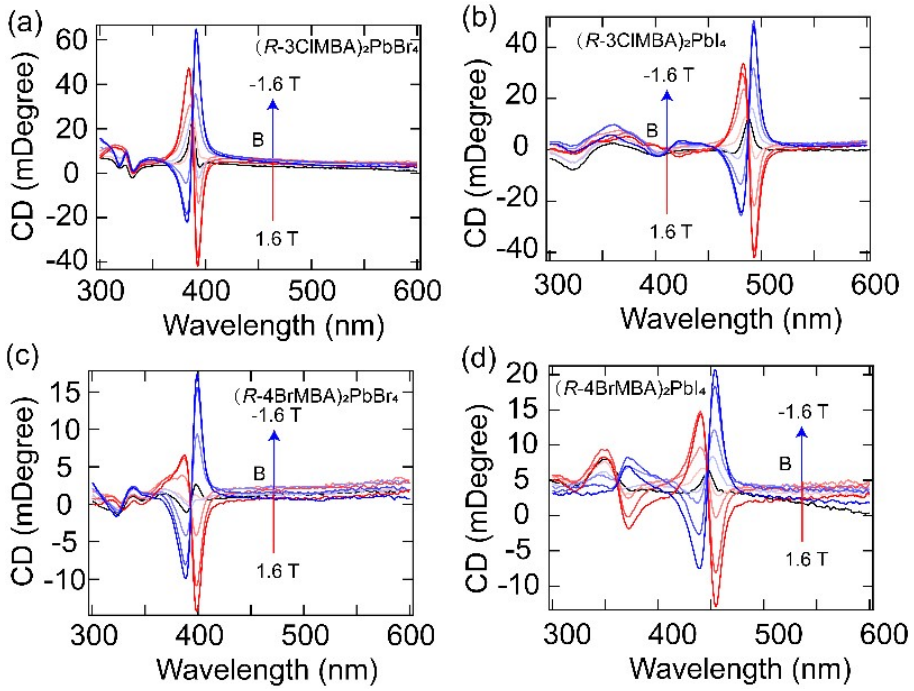

Figure S4. MCD spectra of (a) **(*R*-3ClMBA)$_2$PbBr$_4$**; (b) **(*R*-3ClMBA)$_2$PbI$_4$**; (c) **(*R*-4BrMBA)$_2$PbBr$_4$** and (d) **(*R*-4BrMBA)$_2$PbI$_4$** films under −1.6 T to 1.6 T magnetic field.

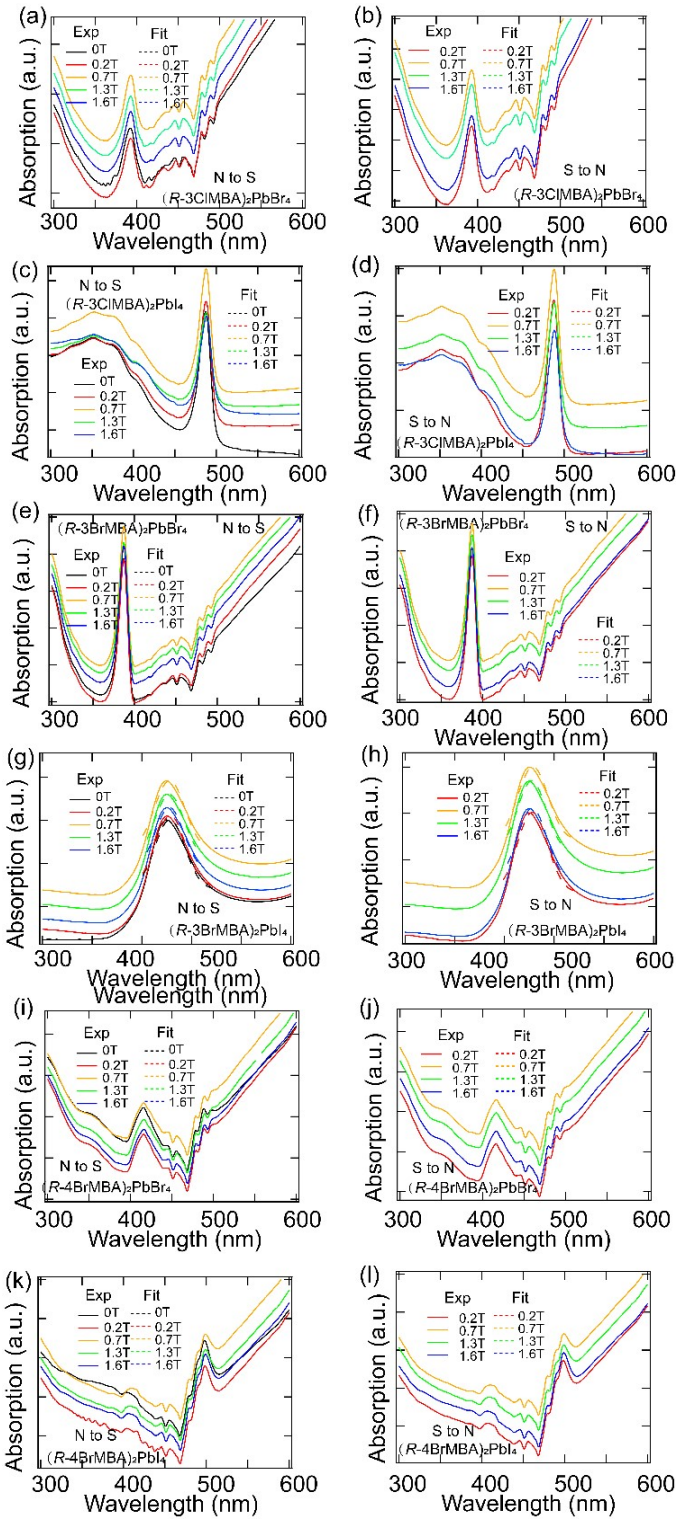

Figure S5. Absorption spectra and the Gaussian fitting curve of the **(*R*-XMBA)$_2$PbX$_4$** films under −1.6 T to 1.6 T magnetic field.

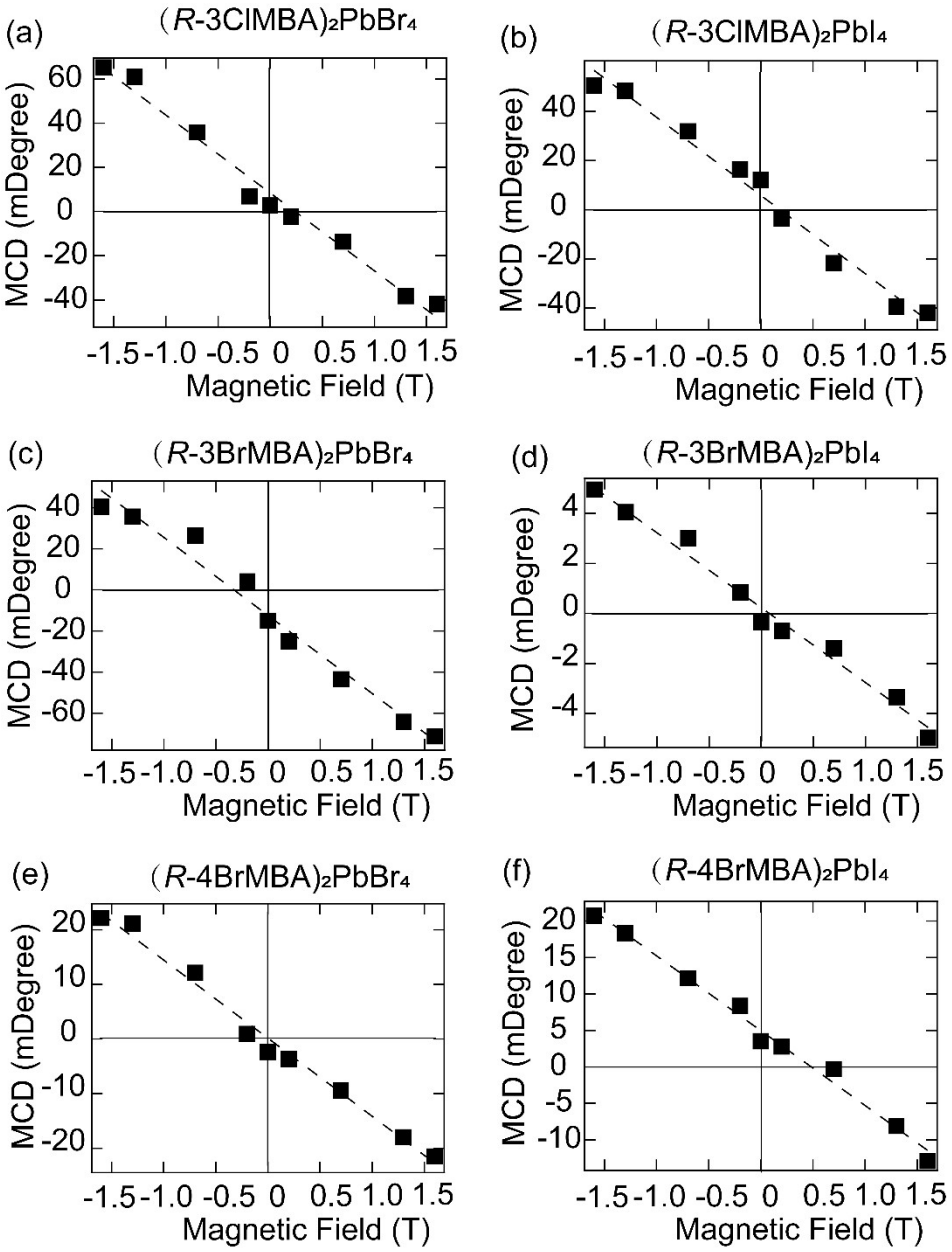

Figure S6. MCD versus external magnetic field and linear fitting curves for samples under −1.6T to 1.6T magnetic field.

Table S4. Zeeman splitting energy calculation for **(*R*-3ClMBA)$_2$PbBr$_4$**.

B(T)	MCD magnitude (mdeg)	Zeeman splitting energy (eV)
-1.6	65.085	0.18488
-1.3	60.937	0.159935
-0.7	35.834	0.089712
-0.2	-2.2661	-0.00666
0	2.7278	0.043622
0.2	6.8909	0.021551
0.7	-13.598	-0.03159
1.3	-38.114	-0.09765
1.6	-41.821	-0.11507

Table S5. Zeeman splitting energy calculation for **(*R*-3ClMBA)$_2$PbI$_4$**.

B(T)	MCD magnitude (mdeg)	Zeeman splitting energy (eV)
-1.6	48.349	0.097376973
-1.3	50.543	0.084579611
-0.7	31.929	0.045367987
-0.2	16.401	0.027453805
0	12.067	0.0076923
0.2	-3.53	-0.0057414
0.7	-21.795	-0.028434479
1.3	-39.553	-0.070088852
1.6	-42.038	-0.074019506

Table S6. Zeeman splitting energy calculation for **(*R*-3BrMBA)$_2$PbBr$_4$**.

B(T)	MCD magnitude (mdeg)	Zeeman splitting energy (eV)
-1.6	40.381	0.15254
-1.3	35.581	0.11835
-0.7	26.54	0.06672
-0.2	4.0762	0.0079
0	-15.001	-0.067
0.2	-25.061	-0.1105
0.7	-43.501	-0.1743
1.3	-64.285	-0.2335
1.6	-71.276	-0.2611

Table S7. Zeeman splitting energy calculation for **(*R*-3BrMBA)$_2$PbI$_4$**.

B(T)	MCD magnitude (mdeg)	Zeeman splitting energy (eV)
-1.6	4.0536	0.052913
-1.3	4.9566	0.026942
-0.7	3.0075	0.022923
-0.2	0.84565	0.018861
0	-0.34897	0.007783
0.2	-0.68733	-0.01293
0.7	-1.3973	-0.0134
1.3	-3.3456	-0.03906
1.6	-4.9747	-0.05482

Table S8. Zeeman splitting energy calculation for **(*R*-4BrMBA)$_2$PbBr$_4$**.

B(T)	MCD magnitude (mdeg)	Zeeman splitting energy (eV)
-1.6	22.14	0.090655367
-1.3	21.126	0.070951572
-0.7	12.094	0.039450831
-0.2	0.90989	0.003938611
0	-2.3454	-0.010119294
0.2	-3.666	-0.015251613
0.7	-9.4571	-0.031592251
1.3	-17.968	-0.06426851
1.6	-21.515	-0.080557896

Table S9. Zeeman splitting energy calculation for **(*R*-4BrMBA)$_2$PbI$_4$**.

B(T)	MCD magnitude (mdeg)	Zeeman splitting energy (eV)
-1.6	20.774	0.049509
-1.3	18.363	0.038359
-0.7	12.166	0.024182
-0.2	8.3643	0.023246
0	3.5299	-0.003729
0.2	2.7894	0.007554
0.7	-0.3009	-0.00064
1.3	-8.1182	-0.01698
1.6	-12.917	-0.02861

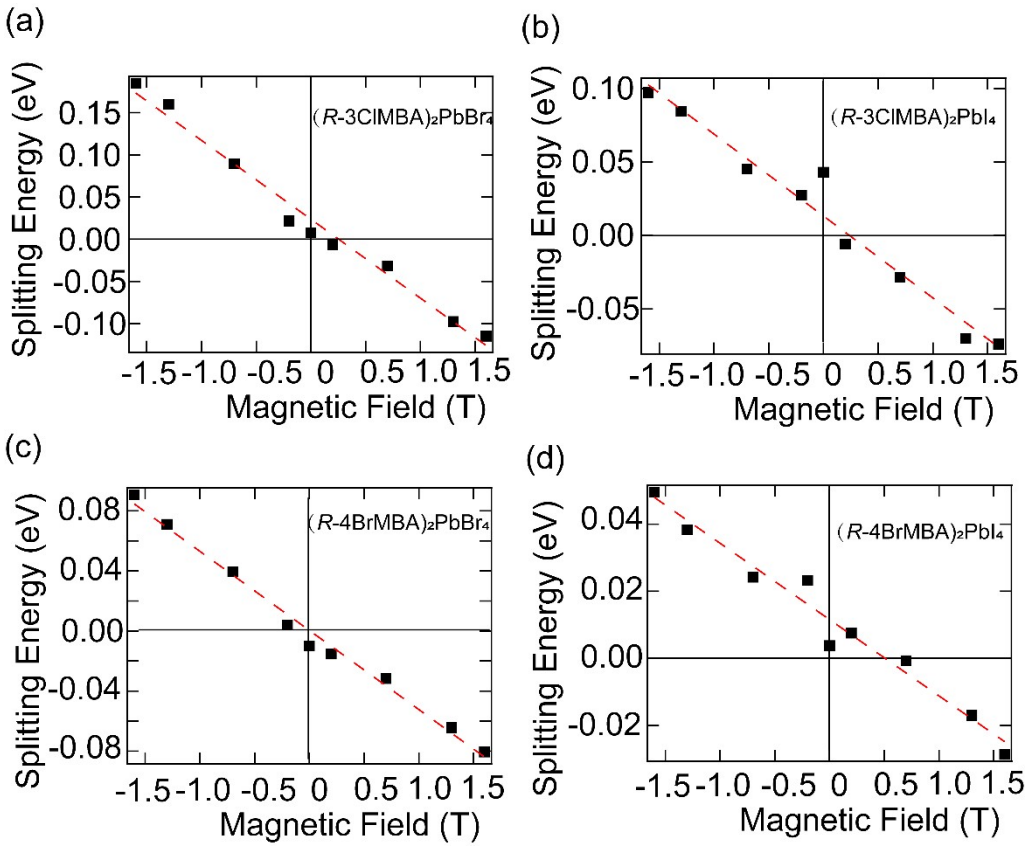

Figure S7. Splitting energy versus external magnetic field and the linear fitting curves for (a) **(*R*-3ClMBA)$_2$PbBr$_4$**; (b) **(*R*-3ClMBA)$_2$PbI$_4$**; (c) **(*R*-4BrMBA)$_2$PbBr$_4$** and (d) **(*R*-4BrMBA)$_2$PbI$_4$** films under −1.6 T to 1.6 T magnetic field.

Table S10. Summary of parameters for quantifying exciton Landé *g* factor and intrinsic splitting energy of the chiral perovskites.

	g_{int} value	Intrinsic field-dependent exciton splitting (eV) ($\times 10^{-3}$)
(*R*-3ClMBA)$_2$PbBr$_4$	1.62	43.6
(*R*-3ClMBA)$_2$PbI$_4$	0.52	7.6
(*R*-3BrMBA)$_2$PbBr$_4$	2.22	67.0
(*R*-3BrMBA)$_2$PbI$_4$	0.96	7.7
(*R*-4BrMBA)$_2$PbBr$_4$	0.90	10.1
(*R*-4BrMBA)$_2$PbI$_4$	0.39	3.7